Spin density waves and ground state helices in EuGa$_{2.4}$Al$_{1.6}$

M. T. Littlehales [1,2,*] S. H. Moody,[3] P. J. Bereciartua,[4] D. A. Mayoh,[5] Z. B. Parkin,[1] T. J. Blundell [6] E. Unsworth,[6]
S. Francoual [4] G. Balakrishnan,[5] D. Alba Venero [2] and P. D. Hatton [1,†]

[1]*Department of Physics, Durham University, South Road, Durham DH1 3LE, United Kingdom*
[2]*ISIS Neutron and Muon Source, Rutherford Appleton Laboratory, Didcot OX11 0QX, United Kingdom*
[3]*Laboratory for Neutron Scattering and Imaging, Paul Scherrer Institute, Villigen CH-5232, Switzerland*
[4]*Deutsches Elektronen-Synchrotron DESY, Notkestraße 85, 22607 Hamburg, Germany*
[5]*Department of Physics, University of Warwick, Coventry CV4 7AL, United Kingdom*
[6]*Department of Chemistry, Durham University, South Road, Durham DH1 3LE, United Kingdom*

The Eu(Ga$_{1-x}$Al$_x$)$_4$ series is composed of centrosymmetric structures which exhibit a wide range of rich topological phenomena, including some members hosting magnetic skyrmions. In this letter, we investigate the previously unreported intermediate compound EuGa$_{2.4}$Al$_{1.6}$, which hosts two distinct phase transitions under zero applied magnetic field. We have used resonant elastic x-ray scattering with full linear polarization analysis to unambiguously determine the zero-field magnetic structures, which consist of a transition between a basal plane transverse spin density wave at higher temperatures into a noncollinear helical ground state. Furthermore, we demonstrate a phase coexistence regime below the transition and reveal an elliptically modulated helical magnetic structure emerging from wavevector splitting.

Among the myriad exotic incommensurate magnetic structures, skyrmions continue to excite the magnetism community [1–5]. Primarily driven by their emergent electromagnetic properties and the discovery of numerous energy-efficient control methods, skyrmions show promise as elements within low-energy spin-based applications [6–14]. Conventionally, they are stabilized by competing direct exchange and the Dzyaloshinskii-Moriya (DM) interactions in noncentrosymmetric helimagnets [15–20]. However, other stabilizing mechanisms including geometric frustration, Rudderman-Kittel-Kasuya-Yosida (RKKY) interactions, and strong spin-lattice coupling have demonstrated a rich variety of skyrmion spin textures in rare-earth-based centrosymmetric intermetallics [21–24]. Recently, a combination of DM and RKKY interactions has been shown to form skyrmion textures with hybrid helicities [25], a prime example of the opportunity provided by combining and tuning the underlying magnetic interactions. Chemical doping allows such an opportunity which has previously resulted in room-temperature skyrmions and a number of exotic low-temperature phases across the CoZnMn series [26]. However, until recently, chemical variation and its effect on emergent physical properties had not been investigated among the centrosymmetric skyrmion materials.

The Eu(Ga$_{1-x}$Al$_x$)$_4$ series provides the first centrosymmetric chemical doping series in which skyrmions are suggested to exist across a number of compositions [27]. Isostructural and electronically similar to GdRu$_2$Si$_2$, an established skyrmion host, Eu(Ga$_{1-x}$Al$_x$)$_4$ crystallizes in the tetragonal $I4/mmm$ space group with a widely varying magnetic phase diagram across the composition series [28]. At one end, EuAl$_4$ hosts numerous incommensurate magnetic phases and metamagnetic transitions, including a vortex lattice, a square to rhombic skyrmion lattice transition, and a helical ground state which switches chirality on reducing temperature [24,29–32]. In contrast, on the far end of the series, EuGa$_4$ hosts a single type A commensurate antiferromagnetic phase [33–36]. In the center, EuGa$_2$Al$_2$ hosts a single intermediate magnetic field phase with a large topological Hall effect (THE), the structure of which is yet to be refined [37]. A variety of different structures have been proposed for the zero-field phases, with suggestions of helix or transverse spin density wave (SDW) transitions into a cycloidal ground state, with varying moment directions [28,38]. Schematics are shown in Fig. 1(c). Additionally, a symmetry breaking charge density wave (CDW) has been shown to be a competing factor in the electronic ordering, leading to complex domain formation and potentially contributing to the THE signal [38]. The variety of different magnetic phases and ground state structures observed across the series is surprising and warrants further study. Naturally, this raises questions as to what happens within the intermediate disordered compounds which have hitherto not been investigated with scattering techniques.

It is with this notion that we bring attention to EuGa$_{2.4}$Al$_{1.6}$ which hosts a multistep transition in zero magnetic field, similar to EuGa$_2$Al$_2$ and EuAl$_4$. Through a comprehensive

---

*Contact author: matthew.t.littlehales@durham.ac.uk
†Contact author: p.d.hatton@durham.ac.uk
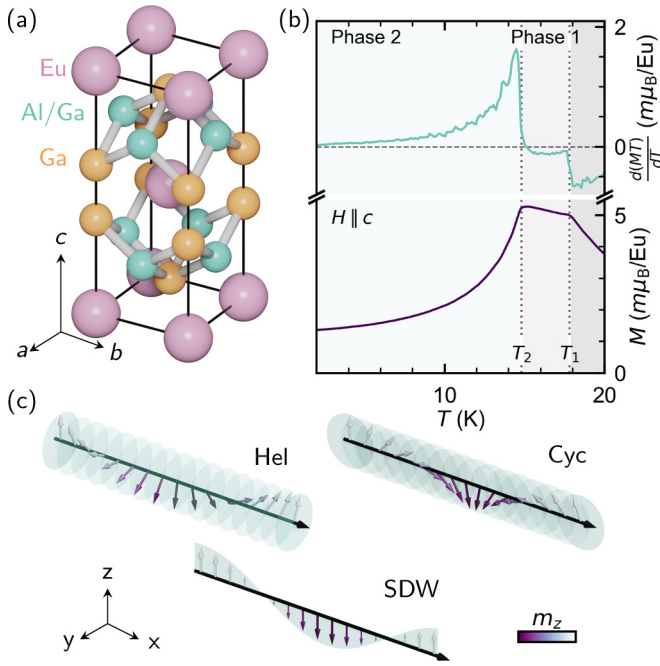
FIG. 1. Crystal structure, characterization, and spin textures. (a) $EuGa_{2.4}Al_{1.6}$ crystal structure with $I4/mmm$ space group. The $4e$ sites are 100% occupied by Ga, whereas $4d$ sites have a 20% occupancy of Al. (b) Low-temperature moment versus temperature (bottom) and temperature derivative $\frac{d(MT)}{d(T)}$ versus temperature (top) indicating two distinct transitions at $T_1 = 17.8$ K and $T_2 = 14.8$ K. Measurements were taken with a 100 Oe field along the c-axis. (c) Reported magnetic structures in the closely associated material, $EuGa_2Al_2$: helix (Hel), cycloid (Cyc), and SDW.

resonant elastic x-ray scattering (REXS) study featuring a full linear polarization analysis (FLPA), we have unambiguously determined the zero-field magnetic textures and the nature of their phase transitions. Our results suggest a transition from a basal plane transverse SDW into a ground state helical phase. In addition, we quantify wavevector splitting on reducing temperature and discuss the possibilities of domain coexistence and structural distortions. In the wider context of the $Eu(Ga_{1-x}Al_x)_4$ series, these measurements suggest a nonmonotonic dependence of the ground state spin structure on the Ga/Al composition and highlight the necessity to refine the magnetic structures across the composition series.

Single crystals of our target material $EuGa_{2.4}Al_{1.6}$ were synthesized using the self-flux technique and characterized with single-crystal x-ray diffraction, confirming the space group and yielding lattice parameters of $a = b = 4.3335(10)$ Å, and $c = 10.8715(5)$ Å at 120 K. The site occupancies were determined from the refinement with perfect gallium occupation on the $4e$ sites and 20% occupation on the $4d$ sites. A representation of the unit cell is shown in Fig. 1(a). Magnetometry measurements in Fig. 1(b) indicate two distinct transitions in both the moment and temperature derivative ($\frac{d(MT)}{dT}$) at $T_1 = 17.8$ K and at $T_2 = 14.8$ K, reflective of a zero-field multistep transition. More details of the characterization can be found within the Supplemental Material [39]. To determine the nature of the two magnetic phases observed within these measurements, we employed high-resolution REXS measurements with FLPA. While neu-

tron diffraction has been the major technique for determining magnetic structures for a number of years [40,41], REXS provides a number of experimental benefits such as element selectivity and overcoming the high neutron absorption of natural europium [42]. More specifically, utilizing FLPA, all components of the magnetization can be resolved to refine the magnetic structure [43–46].

Using the same single crystal, we perform REXS off a polished (1 1 0) face on the P09 resonant scattering and diffraction beamline at the PETRA III synchrotron source in the horizontal scattering geometry with the c-axis aligned vertical, a schematic of which is shown in Fig. 2(a) [47]. A double-phase retarder was used to vary the incoming linear polarization [48] of x-rays tuned to an incident energy close to the Eu L_{II} edge (7.61 keV, Fig. 2(b)). We performed FLPA in combination with a pyrolytic graphite (0 0 6) analyzer crystal by rotating the incoming x-ray polarization and analyzing the scattered x-ray polarization [44]. Using the scattering geometry in Fig. 2(a), the $\pi\sigma'$ or $\sigma\pi'$ scattering channels probe magnetic moments lying within the basal plane while $\pi\pi'$ scattering probes only c-axis components for electric dipole dominated transitions [49,50]. For a more thorough description of resonant x-ray scattering amplitudes, interested readers should see the Supplemental Material [39]. Other than the energy scan in Fig. 2(b), the following measurements are centered around the (2 2 0) Bragg peak and observed under decreasing temperature.

Stark differences are found when comparing h scans within the two magnetic phases [Figs. 2(c) and 2(d)]. Namely, we observe a single magnetic wavevector Q_1 in phase 1, and three collinear wavevectors Q_2, Q_3, Q_4 in phase 2. Differences are also found within the temperature dependence of the integrated intensities in the $\pi\pi'$ and $\pi\sigma'$ scattering channels [Figs. 2(e) and 2(f)], which show the evolution of the wavevector splitting as well as hinting at the nature and origin of each phase. Specifically, the absence of intensity in the $\pi\pi'$ channel indicates a lack of a c-axis component to the spin texture, while any absence in $\pi\sigma'$ would indicate only c-axis components. Intensities in both of the scattering channels were obtained through pseudo-Voigt lineshape fits and plotted in Figs. 2(g) and 2(h), respectively. Similar to the prementioned magnetometry, the REXS intensities display a nonmonotonic temperature dependence with multiple transitions occurring below T_1, namely at $T_2 = 13.5$ K and $T_3 = 11$ K, which are clearly associated with wavevector splitting in Fig. 2(f). The value of T_2 likely differs from the magnetometry due to nominal x-ray beam heating, whereas the transition at T_3 is completely absent in the magnetometry suggesting a more subtle effect. The initial ordering below T_1 shows a single wavevector, Q_1, only in the $\pi\sigma'$ scattering channel, suggestive of a spin texture with moments lying only in the basal plane. At T_2, the wavevector splits into two, whose magnitudes diverge on reducing temperature before a second splitting event at T_3. The polarization dependence of the transitions through T_2 and T_3 suggest that Q_1 and Q_2 are of identical nature, in contrast to Q_3 and Q_4, which both host a more complex spin texture. Since there is little change to the peak positions, the sharp change in intensity at 9 K in Fig. 2(g) may be explained by domain reorientation events between symmetrically equivalent
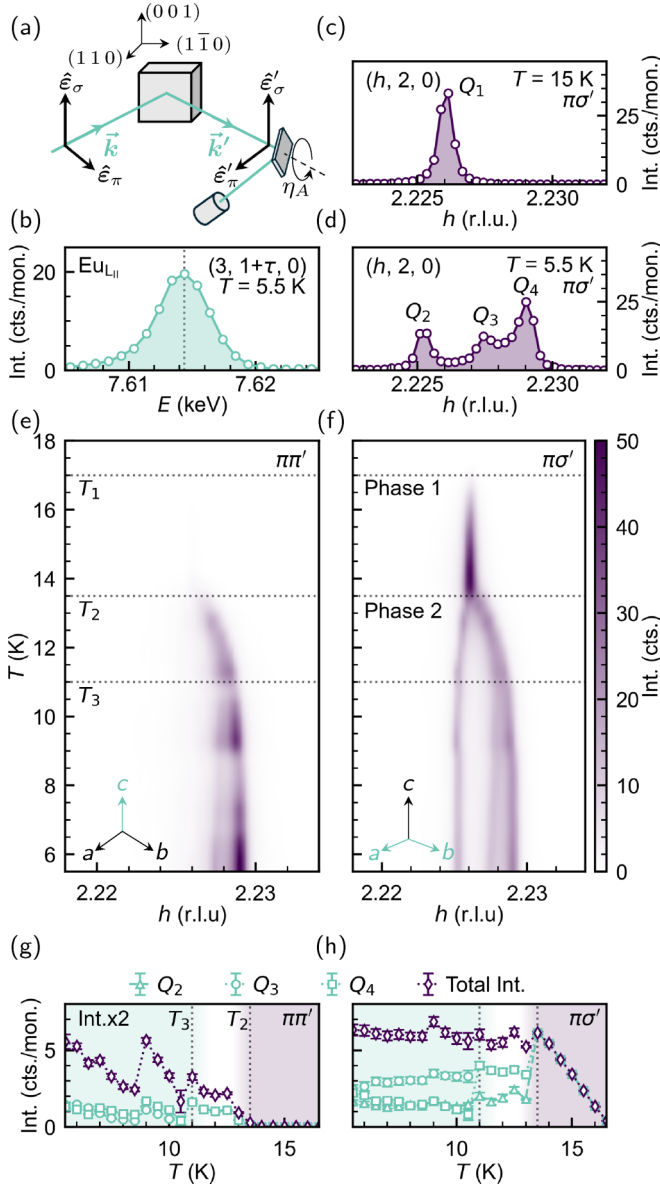
FIG. 2. Temperature-dependent REXS h scans. (a) Scattering schematic indicating the polarization basis with the sample c-axis vertical. (b) Energy scan on the $(3, 1.226, 0)$ magnetic satellite across the Eu L_{II} absorption edge at 5.5 K. (c), (d) h scans at 15 K and 5.5 K respectively measured in the $\pi\sigma'$ scattering channel with corresponding wavevectors indexed by Q_i. (e), (f) Two-dimensional maps of the intensity measured during h scans measured while cooling from 18 to 5.5 K for both the $\pi\pi'$ (e) and $\pi\sigma'$ (f) channels. (g), (h) Integrated h scan intensities as a function of temperature for $\pi\sigma'$ (scaled by 2x) and $\pi\pi'$ channels, respectively.

domains. Consequently, we do not consider this as a fourth transition.

To fully characterize the four observed wavevectors and discern their microscopic nature, we determine the magnetic textures using FLPA. The polarization state of an x-ray beam is fully characterized by the Poincaré-Stokes' parameters $P = (P_1, P_2, P_3)$, where P_1 defines the degree of σ or π polarized light, P_2 the degree of polarized light $\pm 45°$ to the scattering plane, and P_3 the degree of circularly polarized light. For a given incoming polarization angle η_i, the diffracted intensity

TABLE I. Refined model parameters. Best fit irrep combinations and resulting fit parameters (R_y, I_z) for each $(2+\tau, 0, 0)$ type wavevector with corresponding magnetization oblateness, f, and goodness of fit, χ^2. For Q_3/Q_4, R_y is fixed to 1. Allowing it to vary does not lead to improved fit.

Q_i	Irrep	R_y	I_z	f	χ^2
Q_1	mSM3	1.000000(13)	0	–	1.63
Q_2	mSM3	1.000000(14)	0	–	1.95
Q_3	mSM3 & mSM4	1.0	0.826(13)	0.174(13)	6.87
Q_4	mSM3 & mSM4	1.0	0.96(3)	0.04(3)	77.1

from the analyzer crystal is measured as a function of the analyzer crystal rotation, η_A [Fig. 3(a)]. P_1 and P_2 are then extracted from these curves using $I \propto P_1 \sin(2\eta_A) + P_2 \cos(2\eta_A)$ and taking into account cross-talk between polarization channels, resulting in the Stokes' parameters in Fig. 3(b).

First, FLPA of the main beam are measured to determine the degree of linear polarization. FLPA are then measured for Q_i, and the magnetic structure is refined using MagStREXS by taking the main beam Stokes' parameters as an input and determining the structure that transforms them into those of each wavevector. MagStREXS refines the magnetic structure by taking an initial guess from combinations of the basis vectors of the irreducible representations (irreps) allowed by the space group and incommensurate wavevector. For the $(2+\tau, 2, 0)$ wavevector, there are three irreps (mSM2, mSM3, mSM4), which each define an SDW with the moments along the a, b, and c directions, respectively. A general spin texture is described by Fourier components often built from combinations of irreps. The general expression for the Fourier coefficient of a spin texture belonging to wavevector $\boldsymbol{k}$ for an atom j is given by [40]

$$\boldsymbol{S}_{\boldsymbol{k}j} = \tfrac{1}{2}\{\boldsymbol{R}_{\boldsymbol{k}j} + i\boldsymbol{I}_{\boldsymbol{k}j}\} \exp(-2\pi i \phi_{\boldsymbol{k}j}), \qquad (1)$$

where $R = (R_x, R_y, R_z)$, $I = (I_x, I_y, I_z)$ are both real vectors which refer to the proportion of moment oriented along the a, b, and c directions, respectively. $\phi_{\boldsymbol{k}j}$ is a phase parameter useful in describing some magnetic structures but in our case is fixed to zero. As the irreps refer to SDWs along each crystallographic direction, cycloidal and helical spin textures require two irreps (one real and one imaginary), where the relative orientation between the basis vectors and wavevector determines the nature of the spin texture. Using models from combinations of the preceding irreps, clear best fits are observed in the refinement process and are shown in Figs. 3(c)–3(f), with the corresponding models and refinement parameters shown in Table I. For a more thorough explanation of FLPA and the refinement process, alongside examples of poorly fitting magnetic models, see the Supplemental Material [39].

Both Q_1 and Q_2 are well described by a basal plane transverse SDW [Fig. 3(g)], with identical values of R_y and similar goodness of fits, χ^2 (see Table I). In contrast, both Q_3 and Q_4, which only form after T_2 are similarly described by a helical spin structure with the moments in the bc-plane [schematics in Fig. 1(c)]. Any modification of these models does not improve the quality of the fit. Interestingly, the best fit refinements result in a circular helix for Q_4, fulfilling the expected constant moment solution for a ground state structure [52]. However,
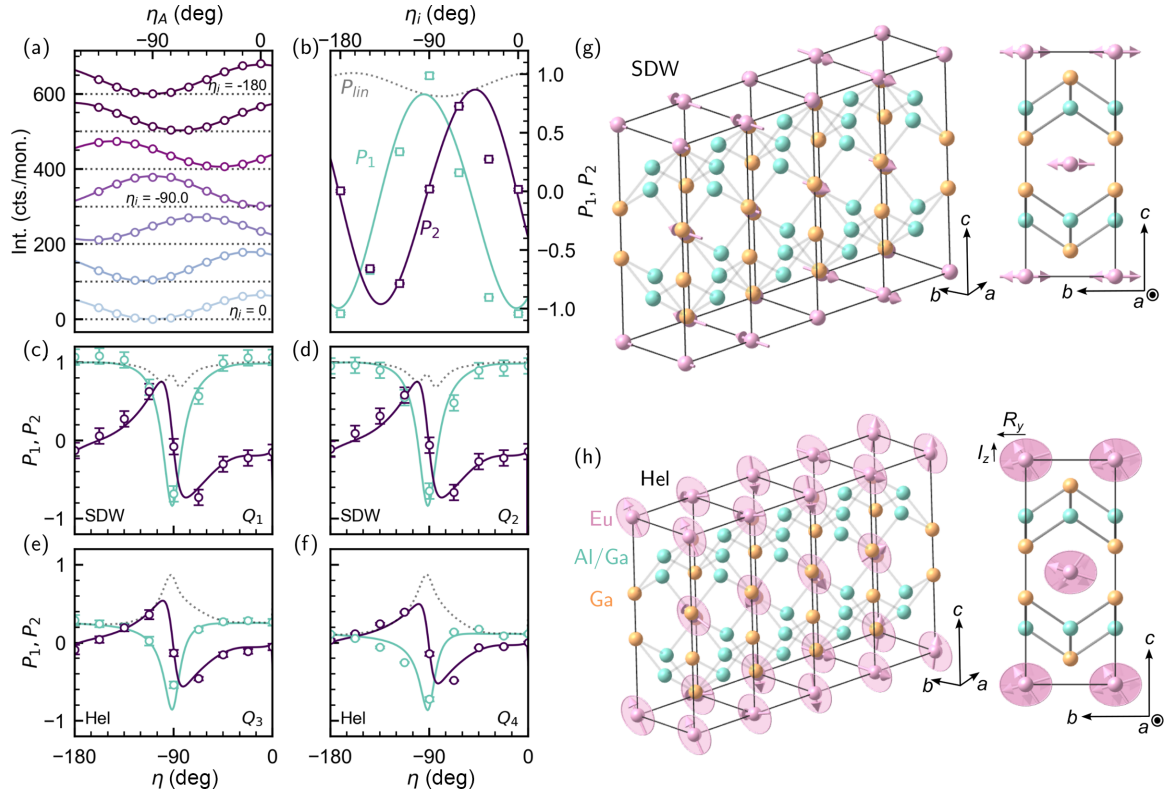
FIG. 3. Full linear polarization analysis. (a) η_A scans of the analyzer crystal for different incoming x-ray polarization fitted with $I \propto P_1\sin(2\eta_A) + P_2\cos(2\eta_A)$. (b) Resulting Stokes parameters P_1 (teal), P_2 (purple) of the main beam for different incoming polarizations. The gray dotted line indicates degree of linearity, $P_{lin} = \sqrt{P_1^2 + P_2^2}$. (c)–(f) Fitted Stokes parameters of each of the four magnetic satellites indicated in Fig. 2(d) using MagStREXS. Q_1 and Q_2 [(c) and (d)] are fit with a basal plane transverse SDW. Q_3 and Q_4 [(e) and (f)] are fit with a helix (Hel). (g), (h) Real space representations of the magnetic structures of Q_1 and Q_3, respectively, plotted over four unit cells using Mag2Pol [51].

the fit of Q_3 shows an elliptical modulation to the helix with an oblateness ($f = \frac{R_y - I_z}{R_y}$, which characterizes the envelope of the helix) of $f = 0.17(3)$, unexpected for a ground state structure. A real space schematic of the elliptically modulated helix for Q_3 is shown in Fig. 3(h). Amplitude modulated spin structures are energetically unfavorable at the low temperature limit leading to commensurate lock-in transitions, squaring up of the magnetization via higher-order harmonic formation, or first-order transitions to a constant moment phase [40,52,53]. These results are consistent with the latter, where the constant moment helical ground state is obtained for Q_4 suggesting a complex mechanism responsible for the elliptical modulation of Q_3.

There are some notable comparisons between these results and those of EuGa$_2$Al$_2$, which similarly displays three distinct transitions on reducing temperature. First, the onset of a basal plane SDW from the paramagnetic phase is identical to the recent REXS results on EuGa$_2$Al$_2$, consistent with a second-order phase transition [38]. Second, the AFM2 phase in EuGa$_2$Al$_2$ is limited between 10.5 and 15.5 K and is considered as mixed phase coexistence. This alone describes the three transitions observed in the magnetometry data: paramagnetic to SDW, SDW to a mixed phase, and mixed phase to a helical ground state. In the case of EuGa$_{2.4}$Al$_{1.6}$, we do not observe a third transition and instead find a phase coexistence regime extending down

to the lowest temperatures measured. Coexistence regions usually surround a first-order phase transition; however, the extent in EuGa$_{2.4}$Al$_{1.6}$ is more than double that observed in EuGa$_2$Al$_2$ [38] suggesting disorder broadening of the transition, which is supported by the minimal residual resistivity ratio in the series found at $x \approx 0.3$ [27]. Lower temperature measurements may elucidate the full range of the disorder broadening.

The elliptical distortion of Q_3 and wavevector splitting absent in the magnetometry poses an interesting question about the nature of the phase. A potential explanation for the Q_3/Q_4 peak splitting could be the formation of a multi-Q spin texture defined by two inequivalent wavevectors. The resulting peak splitting would generate two symmetrically equivalent domains rotated by 90°, and the formation of higher-order harmonics would compensate for the modulated spin structure. An example of this is demonstrated in GdRu$_2$Si$_2$ where higher-order satellites are observed at the $q_1 + 2q_2$ positions resulting in a constant moment ground state and one-dimensional topological charge stripes [54]. However, our zero-field single-crystal neutron diffraction data show no higher-order wavevectors at any integer sum of Q_3 and Q_4 [39], suggesting that multi-Q spin texture formation is unlikely.

Another explanation of the splitting is an orthorhombic crystal distortion, which has been previously observed within

other compositions in the series [31,38,55]. Additional Bragg peaks have been found at specific sample surface locations in $EuGa_2Al_2$, which are indicative of complex domain formation suggested to result from the symmetry breaking CDW [38]. However, we observed no structural distortions down to 20 K and no signatures of CDW formation within this material, in agreement with other disordered compounds across the series [27,39], which is likely caused by the disorder on the Al sites which are suggested to be the main factor in the CDW formation [38]. Consequently, this suggests an alternate mechanism for the domain formation. Interestingly, an orthorhombic distortion has been determined to be a contributor to the skyrmion formation in $EuAl_4$ [31,56], and therefore its presence may be indicative of skyrmion formation across the series. A thorough low-temperature crystal structure determination would determine changes in the unit cell which may be caused by the competing magnetic order.

Within the wider context of the series, the varying magnetic ground state is particularly interesting. $EuGa_4$, $EuGa_2Al_2$, and $EuAl_4$ host commensurate antiferromagnetic, incommensurate cycloid, and incommensurate helical ground states, respectively. Therefore, the resurgence of a helical spin texture with increased Ga substitution suggests a nonmonotonic variation in the ground state across the series. This could be explained by the nonlinear dependence of the Eu-Eu spacing given by the changing lattice parameter and subsequent exchange interaction across the series [27]. Refinements of the structures in $EuAl_4$ have also demonstrated similar elliptical modulations to the helix ground states ($f = 0.286$), with the dipolar interaction suggested to contribute to the favored moment directions [57]. However, since the dipolar energy provides a minor contribution (on the order of $\sim$1 K), a more significant anisotropic interaction is expected to be responsible for the varying ground state and elliptical modulation. A potential explanation is the strong spin-lattice coupling responsible for the skyrmion instabilities in this material [31]. However, without thorough structural characterization as a function of temperature, the responsible mechanism is elusive at this stage. Nevertheless, the similarities in ground state between $EuGa_{2.4}Al_{1.6}$ and $EuAl_4$ highlight the surprising formation of a cycloid in $EuGa_2Al_2$, and call for further scattering studies across the series to provide a more complete understanding of the mechanism responsible for the varying structures.

In summary, we have performed comprehensive REXS measurements with FLPA to determine the nature of the magnetic ground state of $EuGa_{2.4}Al_{1.6}$ and demonstrate complex behavior below the ordering transition resulting in a helical ground state. Compared with the center and end compounds, our results suggest a nonmonotonic variation of the magnetic ground state across the $Eu(Ga_{1-x}Al_x)_4$ series. An investigation of the Al-rich compositions would give more insight into the leading interactions responsible for the varying magnetic ground state, potentially elucidating the requirements for stabilizing topologically nontrivial spin textures. Furthermore, this study highlights the importance of magnetic structure determination, the benefits of REXS with FLPA, and the importance of studying the intermediate compositions within the $Eu(Ga_{1-x}Al_x)_4$ series.

[1] N. Nagaosa and Y. Tokura, Emergent electromagnetism in solids, Phys. Scr. **T146**, 014020 (2012).

[2] N. Nagaosa and Y. Tokura, Topological properties and dynamics of magnetic skyrmions, Nat. Nanotechnol. **8**, 899 (2013).

[3] Y. Tokura and N. Kanazawa, Magnetic skyrmion materials, Chem. Rev. **121**, 2857 (2021).

[4] A. Fert, V. Cros, and J. Sampaio, Skyrmions on the track, Nat. Nanotechnol. **8**, 152 (2013).

[5] C. Back, V. Cros, H. Ebert, K. Everschor-Sitte, A. Fert, M. Garst, T. Ma, S. Mankovsky, T. L. Monchesky, M. Mostovoy, N. Nagaosa, S. S. P. Parkin, C. Pfleiderer, N. Reyren, A. Rosch, Y. Taguchi, Y. Tokura, K. von Bergmann, and J. Zang, The 2020 skyrmionics roadmap, J. Phys. D **53**, 363001 (2020).

[6] F. Jonietz, S. Muühlbauer, C. Pfleiderer, A. Neubauer, W. Münzer, A. Bauer, T. Adams, R. Georgii, P. Boöni, R. A. Duine, K. Everschor, M. Garst, and A. Rosch, Spin transfer torques in MnSi at ultralow current densities, Science **330**, 1648 (2010).

[7] J. S. White, I. Levatić, A. A. Omrani, N. Egetenmeyer, K. Prša, I. Živković, J. L. Gavilano, J. Kohlbrecher, M. Bartkowiak, H. Berger, and H. M. Rønnow, Electric field control of the skyrmion lattice in Cu_2OSeO_3, J. Phys.: Condens. Matter **24**, 432201 (2012).

[8] J. S. White, I. Zivkovic, A. J. Kruchkov, M. Bartkowiak, A. Magrez, and H. M. Rønnow, Electric-field-driven topological phase switching and skyrmion-lattice metastability in magneto-electric Cu_2OSeO_3, Phys. Rev. Appl. **10**, 014021 (2018).

[9] X. Yu, F. Kagawa, S. Seki, M. Kubota, J. Masell, F. S. Yasin, K. Nakajima, M. Nakamura, M. Kawasaki, N. Nagaosa, and Y. Tokura, Real-space observations of 60-nm skyrmion dynamics in an insulating magnet under low heat flow, Nat. Commun. **12**, 5079 (2021).

[10] J. Zázvorka, F. Jakobs, D. Heinze, N. Keil, S. Kromin, S. Jaiswal, K. Litzius, G. Jakob, P. Virnau, D. Pinna, K. Everschor-Sitte, L. Rózsa, A. Donges, U. Nowak, and M. Kläui, Thermal skyrmion diffusion used in a reshuffler device, Nat. Nanotechnol. **14**, 658 (2019).

[11] D. Pinna, G. Bourianoff, and K. Everschor-Sitte, Reservoir computing with random skyrmion textures, Phys. Rev. Appl. **14**, 054020 (2020).

[12] T. Yokouchi, F. Kagawa, M. Hirschberger, Y. Otani, N. Nagaosa, and Y. Tokura, Emergent electromagnetic induction in a helical-spin magnet, Nature (London) **586**, 232 (2020).

[13] G. Berruto, I. Madan, Y. Murooka, G. M. Vanacore, E. Pomarico, J. Rajeswari, R. Lamb, P. Huang, A. J. Kruchkov, Y. Togawa, T. LaGrange, D. McGrouther, H. M. Rønnow, and F. Carbone, Laser-induced skyrmion writing and erasing in an ultrafast cryo-Lorentz transmission electron microscope, Phys. Rev. Lett. **120**, 117201 (2018).

[14] N. T. Bechler and J. Masell, Helitronics as a potential building block for classical and unconventional computing, Neuromorphic Comput. Eng. **3**, 034003 (2023).

[15] A. N. Bogdanov and D. A. Yablonskii, Thermodynamically stable "vortices" in magnetically ordered crystals. The mixed state of magnets, Sov. Phys. JETP **68**, 101 (1989).

[16] S. Mülbauer, B. Binz, F. Jonietz, C. Pfleiderer, A. Rosch, A. Neubauer, R. Georgii, and P. Böni, Skyrmion lattice in a chiral magnet, Science **323**, 915 (2009).

[17] W. Münzer, A. Neubauer, T. Adams, S. Müühlbauer, C. Franz, F. Jonietz, R. Georgii, P. Boöni, B. Pedersen, M. Schmidt, A. Rosch, and C. Pfleiderer, Skyrmion lattice in the doped semiconductor $Fe_{1-x}Co_xSi$, Phys. Rev. B **81**, 041203(R) (2010).

[18] X. Z. Yu, N. Kanazawa, Y. Onose, K. Kimoto, W. Z. Zhang, S. Ishiwata, Y. Matsui, and Y. Tokura, Near room-temperature formation of a skyrmion crystal in thin-films of the helimagnet FeGe, Nat. Mater. **10**, 106 (2011).

[19] S. Seki, X. Z. Yu, S. Ishiwata, and Y. Tokura, Observation of skyrmions in a multiferroic material, Science **336**, 198 (2012).

[20] Y. Tokunaga, X. Z. Yu, J. S. White, H. M. Rønnow, D. Morikawa, Y. Taguchi, and Y. Tokura, A new class of chiral materials hosting magnetic skyrmions beyond room temperature, Nat. Commun. **6**, 7638 (2015).

[21] T. Kurumaji, T. Nakajima, M. Hirschberger, A. Kikkawa, Y. Yamasaki, H. Sagayama, H. Nakao, Y. Taguchi, T. Arima, and Y. Tokura, Skyrmion lattice with a giant topological Hall effect in a frustrated triangular-lattice magnet, Science **365**, 914 (2019).

[22] M. Hirschberger, T. Nakajima, S. Gao, L. Peng, A. Kikkawa, T. Kurumaji, M. Kriener, Y. Yamasaki, H. Sagayama, H. Nakao, K. Ohishi, K. Kakurai, Y. Taguchi, X. Yu, T. Arima, and Y. Tokura, Skyrmion phase and competing magnetic orders on a breathing kagomé lattice, Nat. Commun. **10**, 5831 (2019).

[23] N. D. Khanh, T. Nakajima, X. Yu, S. Gao, K. Shibata, M. Hirschberger, Y. Yamasaki, H. Sagayama, H. Nakao, L. Peng, K. Nakajima, R. Takagi, T. Arima, Y. Tokura, and S. Seki, Nanometric square skyrmion lattice in a centrosymmetric tetragonal magnet, Nat. Nanotechnol. **15**, 444 (2020).

[24] R. Takagi, N. Matsuyama, V. Ukleev, L. Yu, J. S. White, S. Francoual, J. R. L. Mardegan, S. Hayami, H. Saito, K. Kaneko, K. Ohishi, Y. Ōnuki, T. Arima, Y. Tokura, T. Nakajima, and S. Seki, Square and rhombic lattices of magnetic skyrmions in a centrosymmetric binary compound, Nat. Commun. **13**, 1472 (2022).

[25] D. Singh, Y. Fujishiro, S. Hayami, S. H. Moody, T. Nomoto, P. R. Baral, V. Ukleev, R. Cubitt, N.-J. Steinke, D. J. Gawryluk, E. Pomjakushina, Y. Ōnuki, R. Arita, Y. Tokura, N. Kanazawa, and J. S. White, Transition between distinct hybrid skyrmion textures through their hexagonal-to-square crystal transformation in a polar magnet, Nat. Commun. **14**, 8050 (2023).

[26] K. Karube and Y. Taguchi, High-temperature noncentrosymmetric magnets for skyrmionics, APL Mater. **10**, 080902 (2022).

[27] M. Stavinoha, J. A. Cooley, S. G. Minasian, T. M. McQueen, S. M. Kauzlarich, C.-L. Huang, and E. Morosan, Charge density wave behavior and order-disorder in the antiferromagnetic metallic series $Eu(Ga_{1-x}Al_x)_4$, Phys. Rev. B **97**, 195146 (2018).

[28] J. M. Moya, J. Huang, S. Lei, K. Allen, Y. Gao, Y. Sun, M. Yi, and E. Morosan, Real-space and reciprocal-space topology in the $Eu(Ga_{1-x}Al_x)_4$ square net system, Phys. Rev. B **108**, 064436 (2023).

[29] T. Shang, Y. Xu, D. J. Gawryluk, J. Z. Ma, T. Shiroka, M. Shi, and E. Pomjakushina, Anomalous Hall resistivity and possible topological Hall effect in the $EuAl_4$ antiferromagnet, Phys. Rev. B **103**, L020405 (2021).

[30] W. R. Meier, J. R. Torres, R. P. Hermann, J. Zhao, B. Lavina, B. C. Sales, and A. F. May, Thermodynamic insights into the intricate magnetic phase diagram of $EuAl_4$, Phys. Rev. B **106**, 094421 (2022).

[31] M. Gen, R. Takagi, Y. Watanabe, S. Kitou, H. Sagayama, N. Matsuyama, Y. Kohama, A. Ikeda, Y. Ōnuki, T. Kurumaji, T.-H. Arima, and S. Seki, Rhombic skyrmion lattice coupled with orthorhombic structural distortion in $EuAl_4$, Phys. Rev. B **107**, L020410 (2023).

[32] H. Miao, J. Bouaziz, G. Fabbris, W. R. Meier, F. Z. Yang, H. X. Li, C. Nelson, E. Vescovo, S. Zhang, A. D. Christianson, H. N. Lee, Y. Zhang, C. D. Batista, and S. Blügel, Spontaneous chirality flipping in an orthogonal spin-charge ordered topological magnet, Phys. Rev. X **14**, 011053 (2024).

[33] A. Nakamara *et al.*, Magnetic and Fermi surface properties of $EuGa_4$, J. Phys. Soc. Jpn. **82**, 104703 (2013).

[34] M. Yogi, S. Nakamura, N. Higa, H. Niki, Y. Hirose, Y. Ōnuki, and H. Harima, ^{153}Eu and $^{69,71}Ga$ zero-field NMR study of antiferromagnetic state in $EuGa_4$, J. Phys. Soc. Jpn. **82**, 103701 (2013).

[35] T. Kawasaki, K. Kaneko, N. Aso, A. Nakamura, M. Hedo, T. Nakama, Y. Ōnuki, T. Ohhara, R. Kiyanagi, K. Oikawa, I. Tamura, A. Nakao, K. Munakata, and T. Hanashima, Single crystal neutron diffraction study of high neutron absorbing compound $EuGa_4$, JPS Conf. Proc. **2**, 014009 (2014).

[36] T. Kawasaki, K. Kaneko, A. Nakamura, N. Aso, M. Hedo, T. Nakama, T. Ohhara, R. Kiyanagi, K. Oikawa, I. Tamura, A. Nakao, K. Munakata, T. Hanashima, and Y. Ōnuki, Magnetic structure of divalent europium compound $EuGa_4$ studied by single-crystal time-of-flight neutron diffraction, J. Phys. Soc. Jpn. **85**, 114711 (2016).

[37] J. M. Moya, S. Lei, E. M. Clements, C. S. Kengle, S. Sun, K. Allen, Q. Li, Y. Y. Peng, A. A. Husain, M. Mitrano, M. J.

Krogstad, R. Osborn, A. B. Puthirath, S. Chi, L. Debeer-Schmitt, J. Gaudet, P. Abbamonte, J. W. Lynn, and E. Morosan, Incommensurate magnetic orders and topological Hall effect in the square-net centrosymmetric $EuGa_2Al_2$ system, Phys. Rev. Mater. **6**, 074201 (2022).

[38] A. M. Vibhakar, D. D. Khalyavin, J. M. Moya, P. Manuel, F. Orlandi, S. Lei, E. Morosan, and A. Bombardi, Competing charge and magnetic order in the candidate centrosymmetric skyrmion host $EuGa_2Al_2$, Phys. Rev. B **108**, L100404 (2023).

[39] See Supplemental Material at http://link.aps.org/supplemental/10.1103/PhysRevResearch.6.L032015 for details of sample preparation, details of the experimental methods, resonant x-ray scattering formalism, and an account of the fitting procedures used within this study.

[40] J. Rossat-Mignod, Magnetic structures, in *Methods in Experimental Physics: Neutron Scattering*, edited by K. Skoöld and D. L. Price (Academic Press, Cambridge, MA, 1987), Vol. 23, pp. 69–157.

[41] J. Rodríguez-Carvajal, Recent advances in magnetic structure determination by neutron powder diffraction, Phys. B: Condens. Matter **192**, 55 (1993).

[42] E. Beaurepaire, H. Bulou, F. Scheurer, and K. Jean-Paul, *Magnetism and Synchrotron Radiation: New Trends*, Springer Proceedings in Physics (Springer, Berlin, Germany, 2010).

[43] C. Mazzoli, S. B. Wilkins, S. Di Matteo, B. Detlefs, C. Detlefs, V. Scagnoli, L. Paolasini, and P. Ghigna, Disentangling multipole resonances through a full x-ray polarization analysis, Phys. Rev. B **76**, 195118 (2007).

[44] P. D. Hatton, R. D. Johnson, S. R. Bland, C. Mazzoli, T. A. Beale, C. H. Du, and S. B. Wilkins, Magnetic structure determination using polarised resonant x-ray scattering, J. Magn. Magn. Mater. **321**, 810 (2009).

[45] S. R. Bland, B. Detlefs, S. B. Wilkins, T. A. W. Beale, C. Mazzoli, Y. Joly, P. D. Hatton, J. E. Lorenzo, S. D. Brown, and V. A. M. Brabers, Resonant x-ray scattering and full polarisation analysis of forbidden half-integer reflections in magnetite, J. Phys.: Conf. Ser. **211**, 012009 (2010).

[46] W. Simeth, A. Bauer, C. Franz, A. Aqeel, P. J. Bereciartua, J. A. Sears, S. Francoual, C. H. Back, and C. Pfleiderer, Resonant elastic x-ray scattering of antiferromagnetic superstructures in $EuPtSi_3$, Phys. Rev. Lett. **130**, 266701 (2023).

[47] J. Strempfer, S. Francoual, D. Reuther, D. K. Shukla, A. Skaugen, H. Schulte-Schrepping, T. Kracht, and H. Franz, Resonant scattering and diffraction beamline P09 at PETRA III, J. Synchrotron Radiat. **20**, 541 (2013).

[48] S. Francoual, J. Strempfer, D. Reuther, D. K. Shukla, and A. Skaugen, Double phase-retarder set-up at beamline P09 at PETRA III, J. Phys.: Conf. Ser. **425**, 132010 (2013).

[49] J. P. Hill and D. F. McMorrow, X-ray resonant exchange scattering: Polarization dependence and correlation function, Acta Cryst. **52**, 236 (1996).

[50] C. Detlefs, M. S. del Rio, and C. Mazzoli, X-ray polarization: General formalism and polarization analysis, Eur. Phys. J.: Spec. Top. **208**, 359 (2012).

[51] N. Qureshi, *Mag2Pol*: A program for the analysis of spherical neutron polarimetry, flipping ratio and integrated intensity data, J. Appl. Crystallogr. **52**, 175 (2019).

[52] Y. A. Izyumov, Modulated, or long-periodic, magnetic structures of crystals, Sov. Phys. Usp. **27**, 845 (1984).

[53] T. Chattopadhyayand P. J. Brown, Neutron diffraction study of the magnetic (H,T) phase diagrams of $EuAs_3$ and $Eu(As_{1-x}P_x)_3$, Phys. Rev. B **38**, 350 (1988).

[54] G. D. A. Wood, D. D. Khalyavin, D. A. Mayoh, J. Bouaziz, A. E. Hall, S. J. R. Holt, F. Orlandi, P. Manuel, S. Blügel, J. B. Staunton, O. A. Petrenko, M. R. Lees, and G. Balakrishnan, Double-q ground state with topological charge stripes in the centrosymmetric skyrmion candidate $GdRu_2Si_2$, Phys. Rev. B **107**, L180402 (2023).

[55] S. Ramakrishnan, S. R. Kotla, T. Rekis, J.-K. Bao, C. Eisele, L. Noohinejad, M. Tolkiehn, C. Paulmann, B. Singh, R. Verma, B. Bag, R. Kulkarni, A. Thamizhavel, B. Singh, S. Ramakrishnan, and S. van Smaalen, Orthorhombic charge density wave on the tetragonal lattice of $EuAl_4$, IUCrJ **9**, 378 (2022).

[56] S. Hayami, Orthorhombic distortion and rectangular skyrmion crystal in a centrosymmetric tetragonal host, J. Phys. Mater. **6**, 014006 (2023).

[57] A. M. Vibhakar, D. D. Khalyavin, F. Orlandi, J. M. Moya, S. Lei, E. Morosan, and A. Bombardi, Spontaneous spin chirality reversal and competing phases in the topological magnet $EuAl_4$, arXiv:2403.10159 [cond-mat.str-el].

[58] M. T. Littlehales, S. H. Moody, P. J. Bereciartua, D. A. Mayoh, Z. B. Parkin, T. J. Blundell, E. Unsworth, S. Francoual, G. Balakrishnan, D. Alba Venero, and P. D. Hatton, Spin density waves and ground state helices in $EuGa_{2.4}Al_{1.6}$ [dataset], Durham University, doi: 10.15128/r21z40ks89k